Journal of MATERIALS RESEARCH

Article
DOI: 10.1557/jmr.2019.7

Effect of processing parameters on thermal behavior and related density in GH3536 alloy manufactured by selective laser melting

Liang Zhang[1], Jia Song[2,a], Wenheng Wu[3,b], Zhibin Gao[4], Beibei He[3], Xiaoqing Ni[2], Qianlei Long[3], Lin Lu[3], Guoliang Zhu[5]

[1]*Shanghai Engineering Research Center of 3D Printing Materials, Shanghai Research Institute of Materials, Shanghai 200437, China*
[2]*Shanghai Engineering Research Center of 3D Printing Materials, Shanghai 200437, China*
[3]*Shanghai Research Institute of Materials, Shanghai 200437, China*
[4]*Center for Phononics and Thermal Energy Science, China-EU Joint Center for Nanophononics, Shanghai Key Laboratory of Special Artificial Microstructure Materials and Technology, School of Physics Sciences and Engineering, Tongji University, Shanghai 200092, China*
[5]*Shanghai Key Laboratory of Advanced High-temperature Materials and Precision Forming, School of Materials Science and Engineering, Shanghai Jiao Tong University, Shanghai 200240, China*
[a]Address all correspondence to these authors. e-mail: skylve@t.shu.edu.cn
[b]e-mail: wwhwwh2004@126.com

Received: 25 September 2018; accepted: 26 December 2018

GH3536 alloy is one of the high-temperature nickel-based alloys and widely applied in aviation and aerospace industries. In this study, a combination of experiment and simulation is proposed to study the effect of processing parameters on the selective laser melting (SLM) of GH3536 powder. It is concluded that the relationship between density and laser input energy during SLM complies with a quadratic function and presents an inverted U-shaped distribution. By fitting density and input power to a quadratic polynomial, the optimal laser input energy during SLM of GH3536 alloy can be obtained. The result shows that using 275 W laser power and 960 mm/s scanning speed, the SLM GH3536 specimens can reach the maximum density. This experimental result is consistent with the simulation result obtained by analyzing molten pool dimension. Furthermore, a full process energy prediction diagram for SLM GH3536 alloy based on the simulated molten pool depth and width is proposed. The result shows that it provides an innovative and efficient method for the selection of processing parameters during SLM of GH3536 powder.

Introduction

GH3536 alloy, is one of the high-temperature nickel-based alloys, has excellent anti-oxidation, hot corrosion resistance, and superior mechanical performance. Besides, it also possesses satisfactory hot and cold processing formability and can maintain moderate creep strength under 900 °C [1]. Based on these good properties, GH3536 alloy has drawn extensive attention for practical applications in aviation and aerospace industries, for instance, it is suitable to make aviation engine combustion chamber components and other high-temperature parts. Nevertheless, with the rapid development of industrial technology, traditional manufacturing technique for GH3536 components is increasingly incapable of meeting the demand for complex construction design.

In recent decades, selective laser melting (SLM), is one of the major additive manufacturing processes, provides a promising perspective for designing and production of complex components with near net shape [2, 3, 4, 5, 6]. Compared with traditional subtractive manufacturing, SLM technology provides several noticeable advantages, such as decrease in the production procedures, a high level of flexibility, a high material utilization rate, near-net forming, and manufacturing precision parts without the restriction of shapes and materials [7, 8].

So far, a lot of experimental researches have been done, which are related to the process optimization in SLM. Chen et al. [9] designed a set of experiments to investigate the effect of processing parameters (laser power, laser scanning speed,

https://doi.org/10.1557/jmr.2019.7 Published online by Cambridge University Press

© Materials Research Society 2019

and hatching space) on the density of the AlSi10Mg parts manufactured by SLM. To analyze the SLM process integrally, laser energy density was introduced, which is a combination of the above dominant parameters. The experimental results indicated that a high density was obtained by SLM at an optimal laser energy density of 3.5–5.5 J/mm^2. Song et al. [10] used SLM technique to manufacture a series of Ti6Al4V parts with various processing parameters. It was found that the densification and mechanical property of Ti6Al4V parts were a strong function of processing parameters. An excellent Ti6Al4V part could be manufactured by SLM using laser power 110 W and scanning speed 0.4 m/s. Bai et al. [11] manufactured 18Ni-300 maraging steel parts by SLM to investigate the influence of processing parameters on density of these parts. They pointed out that the relative density increased first and then decreased with the laser power, scanning speed, and scanning space. And the maximum relative density was obtained under the optimal processing parameters: laser power of 160 W, scanning speed of 400 mm/s, and scanning space of 0.07 mm.

There are many finite element simulation researches about the SLM technology, as well. Yu et al. [12] established a 3D mesoscopic model to investigate the process of powder-to-solid transition under different processing parameters during the SLM of AlSi10Mg powder. Their results demonstrated that both high and low laser power led to a rough surface quality and the optimal processing parameters were laser power of 250 W, scanning speed of 400 mm/s, and powder layer thickness of 50 μm. Luo et al. [13] proposed a 3D nonlinear transient finite element model to analyze the temperature distribution during the SLM process of thermoelectric SnTe. The calculated results indicated that the molten pool size, the maximum temperature, and the cooling rate increased linearly as the laser power is increased from 8 to 14 W. An opposite trend was observed when the scanning speed is increased from 100 to 400 mm/s. Li et al. [14] developed a 3D finite element model to study the effects of laser power and scanning speed on the thermal behavior during the SLM process of aluminum alloy. It showed that the molten pool size slightly increased as the laser power increased from 150 to 300 W but decreased as the scanning speed increased from 100 to 400 mm/s. The proper molten pool width and depth were 111.4 μm and 67.5 μm, respectively, with the corresponding laser power of 250 W and scanning speed of 200 mm/s.

Both experimental and simulated researches help us to optimize the processing parameters of SLM and reveal the internal mechanism of SLM. On the one hand, the lack of researches about the parameters optimization of GH3536 alloy limits its exemplary application. On the other hand, the systematically predictive ability of process optimization of GH3536 alloy has not yet been developed, because the systematic researches on the processing parameters, temperature distribution, molten pool size, and density are scarce, especially both using experimental study and numerical simulation.

In this research, the influence of processing parameters on the thermal field and density in SLM GH3536 parts is investigated systematically by the combination of experimental study and numerical simulation. The relationship between laser input energy and density of SLM GH3536 part is revealed by experimental study, and the optimal input energy is obtained. In addition, an effective 3D finite element model is proposed to forecast the molten pool dimensions under various processing parameters. The theoretical value of optimal laser energy is acquired via analyzing molten pool dimensions. The simulated result is validated using the experimental results. At last, based on both experimental and simulation results, a full process energy prediction diagram for SLM GH3536 powder is proposed and discussed, which provides an efficient method for selection of process parameters during SLM of GH3536 alloy.

Results and discussion

The microstructure of SLM part and the molten pool shape

The microstructure of GH3536 parts manufactured by SLM with different parameters (laser power and hatching space) is illustrated in Figs. 1–3. When the laser power is less than 100 W or greater 345 W, the sample shows more porosity. This can be attributed to that low input laser power cannot melt powder completely and high laser power may result in the balling effect. Incomplete fusion and balling effect will have a detrimental influence on the density of SLM part. In addition, it is worth noting that when the hatching space is set to 100 μm, pores are usually less than in the case of 70 and 130 μm hatching space. This result is reasonable because the hatching space of GH3536 alloy is often set to 110 μm in some commercial SLM process for Ni-based alloys.

It is also worth noting that the molten pool presents a narrow-long shape in the high laser power cases, as shown in Figs. 1(d)–3(d). This phenomenon seems to conflict with the previous conclusion that the higher the laser power is, the larger the melt pool is. This can be ascribed to the fact that in the high laser power case, the molten pool is large indeed, meanwhile the overlap area between the molten pools is great as well, thus resulting in a narrow-long shape in the final SLM samples. This phenomenon is clearly illustrated in Fig. 4. Moreover, as the hatching space increases, the narrow degree of molten pool in the high laser power decreases. This is because that the overlap area of the molten pool decreases with the increase in the hatching space.

https://doi.org/10.1557/jmr.2019.7 Published online by Cambridge University Press

© Materials Research Society 2019

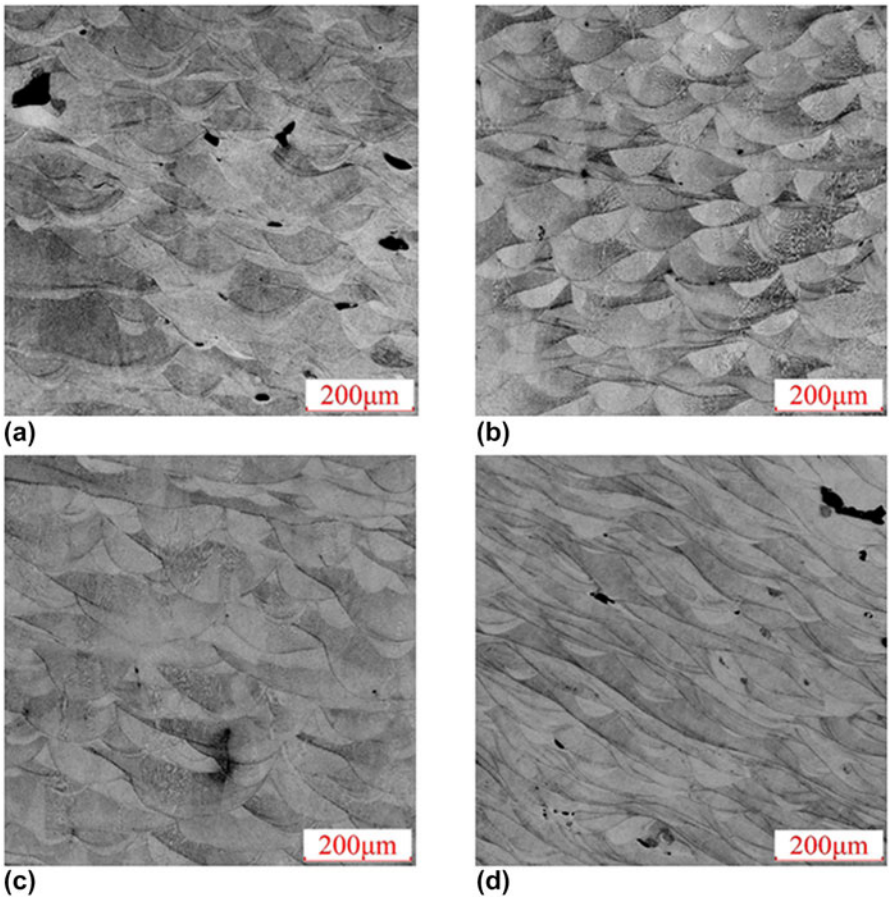


Figure 1: Optical micrographs of SLM-produced GH3536 parts with 70 μm hatching space using different laser power: (a) $P = 100$ W, (b) $P = 200$ W, (c) $P = 285$ W, and (d) $P = 345$ W.

Effect of laser power on the relative density

The relative density is defined as the ratio of measured density to theoretical density. In this study, the theoretical density of GH3536 alloy is 8.358 g/cm^3 [taken from Refs. 15 and 16]. Figure 5 shows the effect of laser power on the relative density of the GH3536 samples fabricated by SLM with a constant scanning speed $v = 960$ mm/s using different powder layer thickness: (a) $d = 40$ μm, (b) $d = 70$ μm, and (c) $d = 100$ μm. The relative density of the fabricated part varies depending on the input laser power and presents an inverted U-shaped distribution in all cases: the relative density increases with increasing the input laser energy, while this is a slight decrease in the high power range. The maximum relative density can be obtained by fitting these dependencies to quadratic polynomials and corresponding power is about 275 W in all cases. This phenomenon can be explained by using following two possible reasons. On the one hand, when the input laser power is below 275 W, the relative density of part is mainly affected by the flow ability of the melt, which is proportional to input laser power and the overlap of melting pool. Very low laser energy results in lack of fusion during SLM, which influences the relative density. On the other hand, when the input power exceeds 275 W, there is a tendency of the balling phenomenon in the SLM process, which is a typical metallurgical defect and will produce a detrimental impact on the relative density of part. Owing to the balling effect, the relative density of part decreases with increasing power in the high power range.

In addition, it also can be found that the relative density of GH3536 parts increases with increasing the hatching space, especially when the applied power is below 200 W. As mentioned above, the overlap of melting pool during SLM is a key factor that affects the relative density. When the hatching space is too small, a large percentage of solidified alloy might be undergo a re-melting procedure, which is caused by nearby laser scanning path. This re-melting procedure might result to the pores formation, especially when the laser power is too low to fully re-melt the solid alloy.

Simulation investigation and discussions

Molten pool dimension plays a crucial role in the SLM process. It significantly affects the metallurgical bonding between the adjacent trajectories and layers during the SLM process. Laser

https://doi.org/10.1557/jmr.2019.7 Published online by Cambridge University Press

© Materials Research Society 2019

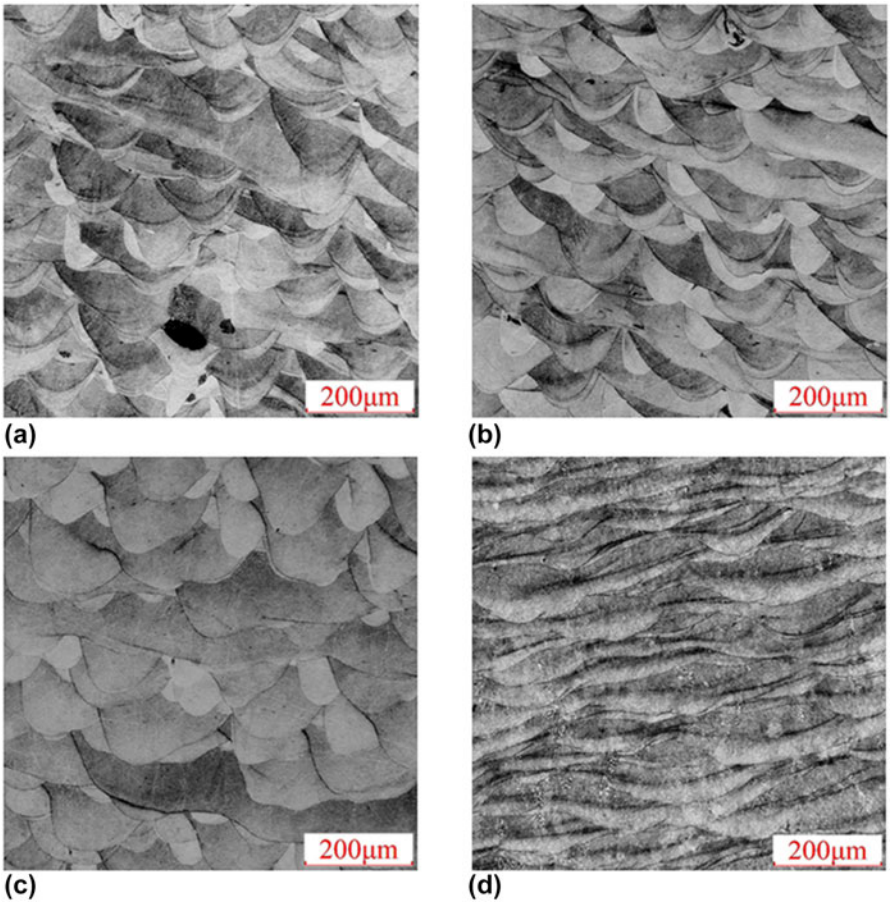


Figure 2: Optical micrographs of SLM-produced GH3536 parts with 100 μm hatching space using different laser power: (a) $P = 100$ W, (b) $P = 200$ W, (c) $P = 285$ W, and (d) $P = 345$ W.

line energy density, ρ_{le}, is a key factor affecting the metallurgical characteristics of products, which can be defined as the ratio of the laser power P to scanning velocity V as follows:

$$\rho_{le} = P/V \quad . \tag{1}$$

It is reported that laser line energy density determines the size of molten pool and other thermal behaviors. Insufficient energy density results in poor metallurgical bonding, thus large amounts of pores are formed. Excessive energy density may lead to balls forming on the surface, which will affect the density as well. If the molten pool size is appropriate, the defect of SLM parts caused by improper thermal input parameter can be avoided, as discussed in the Effect of laser power on the relative density section. Hence, it is indispensable to investigate the molten pool dimension. In this research, an finite element method (FEM) model is used to reveal the effect of different thermal input parameter on melt pool dimension. This model was used in our previous works [17] and validated by the experimental results.

To understand the effect of thermal input parameter on the molten pool dimension systematically, several combinations of laser power (100, 150, 200, 255, 285, 315, 350, 400 W) and scanning speed (660, 860, 960, 1060, 1260, 1560 mm/s), which represent different line energy density, were used.

Figure 6(a) is a summary of all studied cases in the model. As shown in Fig. 6(a), the relationship between laser line energy density and molten pool dimension can be fitted satisfactorily to an exponential function with R^2 values of 0.9868 for molten pool width and 0.9829 for molten pool depth:

$$y = y_0 + A_1 e^{-x/t_1} + A_2 e^{-x/t_2} \quad , \tag{2}$$

where for molten pool width, the y_0, A_1, t_1, A_2, and t_2 are parameters evaluated from our numerical simulation at 366.03, −117.70, 0.07, −341.35, and 1.14, respectively. And for molten pool depth, the y_0, A_1, t_1, A_2, and t_2 are obtained at 101.92, −83.77, 0.32, −82.28, and 0.05, respectively. In general, both width and depth of molten pool increase with increasing the laser line energy density.

In addition, we also investigated the effect of laser energy density, E (J/mm^3), on the molten pool size, which is a measure for the averaged applied energy per volume of material during the scanning of a layer:

https://doi.org/10.1557/jmr.2019.7 Published online by Cambridge University Press

© Materials Research Society 2019

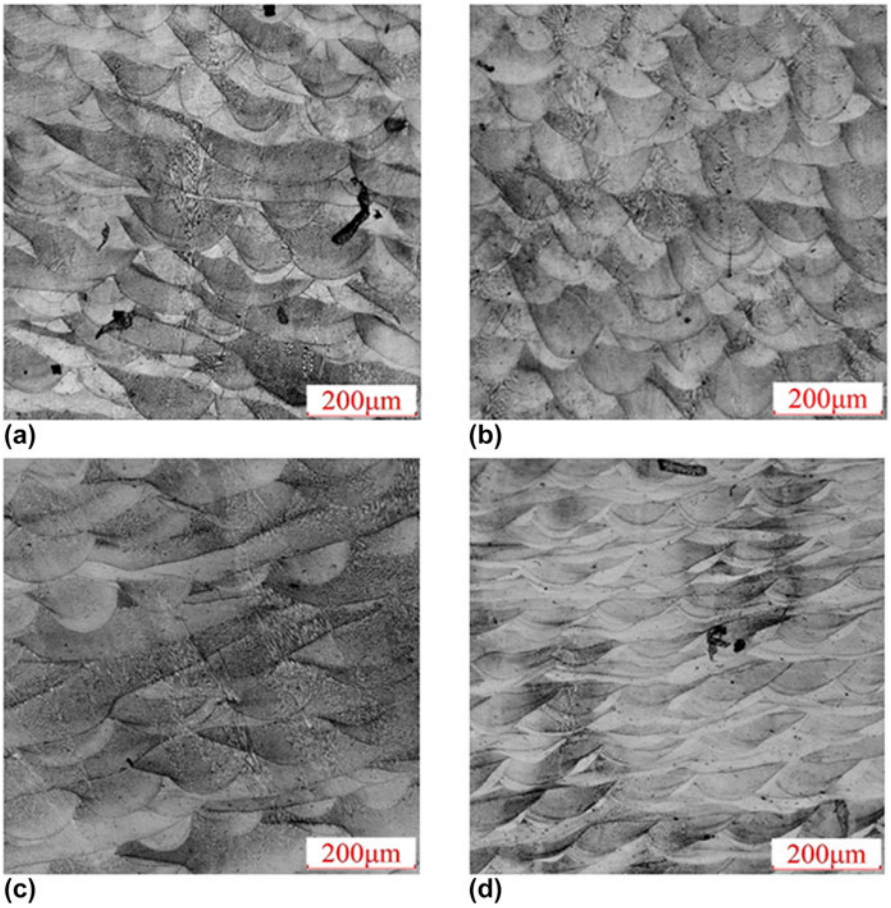


Figure 3: Optical micrographs of SLM-produced GH3536 parts with 130 μm hatching space using different laser power: (a) $P = 100$ W, (b) $P = 200$ W, (c) $P = 285$ W, and (d) $P = 345$ W.

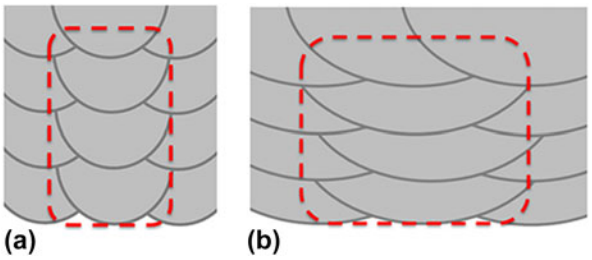


Figure 4: Schematic diagram of molten pool shape at (a) low laser power and (b) high laser power.

$$E = \frac{P}{V \cdot h \cdot t} \quad , \tag{3}$$

where P is the laser power, V is the scanning velocity, h is the hatch spacing, and t is the layer thickness. The effect of energy density on the molten pool size is similar to line energy density, as shown in Fig. 6.

As discussed in the microstructure of SLM part and the molten pool shape section, a proper overlap area between adjacent trajectories and layers is beneficial to avoid the formation of pores during SLM. We can assume that a combination of melt pool width and hatching space is mainly to control the overlap area between adjacent trajectories in the same layer, while a combination of melt pool depth and powder layer thickness is mainly to control the overlap area between vertical trajectories in different layers. Keeping this assumption in mind, it is interesting to draw a full process energy prediction diagram for SLM GH3536 alloy based on the simulated melt pool dimension, as shown in Fig. 7.

In Fig. 7(a), the powder layer thickness is set to constant 40 μm, the data points represent the simulated melt pool width under the different laser scanning speed and laser power. Several contour lines can be drawn, which represent the same level of melt pool width, such as blue lines in Fig. 7(a). These blue lines represent 70 μm melt pool width and 105 μm melt pool width. Based on this diagram, an efficient method for hatching space selection can be proposed. For instance, if a scanning speed of 960 mm/s and a laser power of 280 W are used, the corresponding melt pool width is about 105 μm, the best hatching space will be about 70 μm to overlap 1/2 melt pool to reach a good metallurgical bonding. This prediction is

https://doi.org/10.1557/jmr.2019.7 Published online by Cambridge University Press

© Materials Research Society 2019

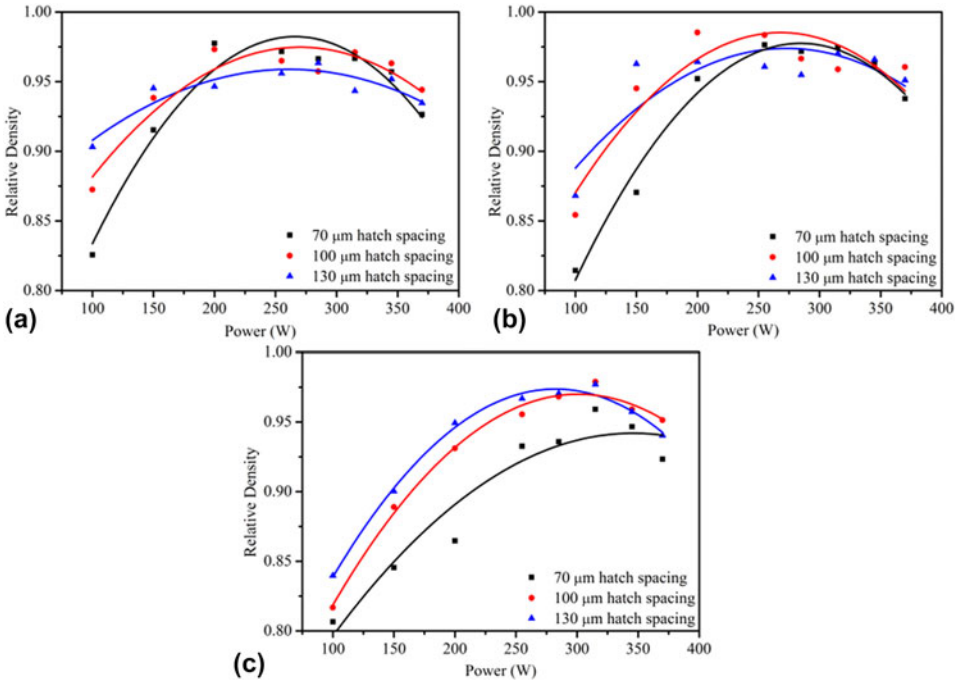


Figure 5: Effect of laser power on density of GH3536 SLM parts under different powder layer thickness (v = 960 mm/s): (a) d = 40 μm, (b) d = 70 μm, and (c) d = 100 μm.

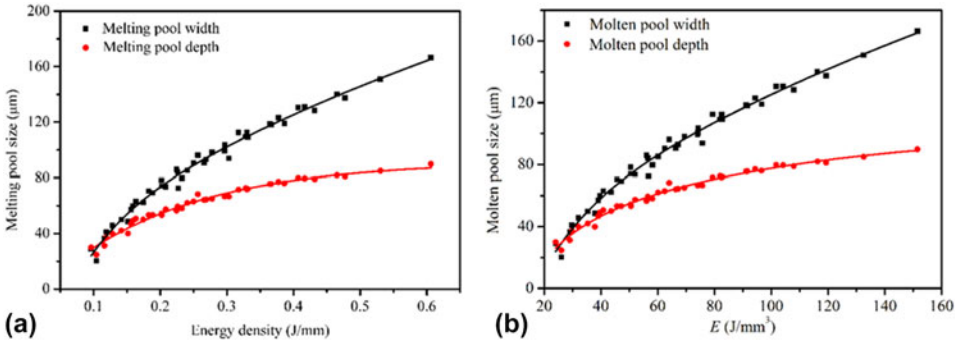


Figure 6: Effect of (a) laser line energy density and (b) energy density on the simulated melting pool in this research.

in good agreement with our experimental results, as shown in Fig. 5(a). This method also can be used for selection of laser scanning speed and laser power in a similar way.

Similarly, if the hatching space is set to constant 70 μm, a full process energy prediction diagram for SLM GH3536 alloy powder layer thickness can be drawn, as shown in Fig. 7(b). The data points here represent the simulated melt pool depth under the different laser scanning speed and laser power. Several contour lines can be drawn, which represent the same level of melt pool depth, such as blue lines in Fig. 7(b). These blue lines represent 40 μm powder layer thickness and 60 μm powder layer thickness. Based on this diagram, for instance, if a scanning speed 960 mm/s and a laser power 240 W are used, the corresponding melt pool depth is about 60 μm, the best powder layer will be about 40 μm to overlap 1/2 melt pool in vertical direction to reach a good metallurgical bonding between layers. This prediction can be confirmed by the experimental result in Fig. 5(a).

In summary, the proposed process energy prediction diagram in this research provides an innovative and efficient method for the selection of thermal parameters during SLM process of GH3536 alloy.

Conclusions

In this research, the influence of processing parameters on the thermal field and density in SLM GH3536 parts is investigated systematically by the combination of experimental study and numerical simulation. First, the microstructure and density of GH3536 components are studied by experimental method.

https://doi.org/10.1557/jmr.2019.7 Published online by Cambridge University Press

© Materials Research Society 2019

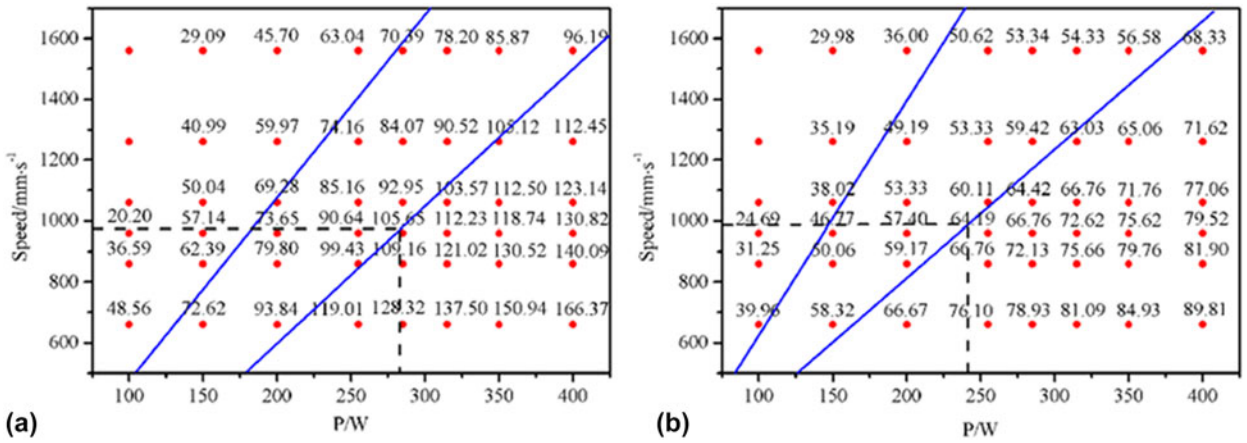


Figure 7: A full process energy prediction diagram for SLM GH3536 alloy based on the simulated (a) melt pool width and (b) melt pool depth. The blue lines from left to right represent 70 μm and 105 μm melt pool width in (a) and 40 μm and 60 μm melt pool depth in (b). The red data points indicate the simulated melt pool width under the different laser scanning speed and laser power.

Second, a three-dimensional finite model of the SLM process is proposed to further study the effect of thermal parameters on the thermal behavior and melt pool dimension during SLM. In addition, a full process energy prediction diagram for SLM GH3536 alloy based on the simulated melt pool depth and width is proposed. The following conclusions can be drawn in this research.

(1) The density increases with increasing the input laser energy, while this is a slight decrease in the high power range. The maximum density can be obtained using 275 W laser power and 960 mm/s scanning speed. This is due to lack of fusion under the low laser energy and balling effect under high laser power range.
(2) The relationship between laser line energy density and molten pool dimension obeys the exponential function. In general, both width and depth of molten pool increase with increasing the laser line energy density.
(3) Although the proposed process energy prediction diagram in this research is based on the simulated results, it provides an innovative and efficient method for the selection of thermal parameters during SLM process of GH3536 alloy.

Experimental procedures

The samples used in this research were fabricated using an EOS M290 SLM machine (EOS, Munich, Germany). The size of samples was 1 × 1 × 1 cm. The raw material is Ni-based GH3536 alloy spherical powders, which is in the range of 15–53 m. The chemical composition of GH3536 powder is listed as follows (mass fraction %): 0.45 Si, 21.45 Cr, 18.99 Fe, 4.03 V, 8.73 Mo, 0.45 Mn, 0.99 Co, 0.52 W, and balance Ni.

TABLE I: The parameters of SLM used in this research.

Parameter	Value
Powder layer thickness, *d*	40, 70, and 100 μm
Hatching space, *s*	70, 100, and 130 μm
Laser power, *P*	100, 150, 200, 255, 285, 315, 345, and 370 W

The EOS M290 SLM machine used in this research consists of a fiber laser beam with a maximum power of 400 W and a spot diameter of 80–150 μm. During SLM processing, the stainless steel substrate is preheated to 200 °C, and the scanning speed is fixed at 960 mm/s in all experimental studied cases. That is attributed to that 960 mm/s is not only the typical operation scanning speed in the SLM GH3536 powder but also ensures the stable formation of GH3536 powder. The powder layer thickness, deposition hatching space and laser power are varied in experimental research and are listed in Table I.

After fabrication, the density of samples is measured using an automatic density meter, which is based on Archimedes principle. All SLM samples are ground and polished first, then slightly eroded with an aqua regia (nitric acid:hydrochloric acid = 1:3) according to a standard metallographic procedure. The cross-sectional microstructure of the eroded part is examined using an optical microscope.

Finite element modeling method

Thermal modeling

Considering the laser penetration and the transient thermal transportation phenomenon in the SLM process, a modified Gaussian body heat source distribution is used in this research, as suggested in many researches [18, 19, 20, 21] and our previous works [17]:

https://doi.org/10.1557/jmr.2019.7 Published online by Cambridge University Press

© Materials Research Society 2019

$$q(x,y,z) = \frac{\eta \cdot 6\sqrt{3}Q}{hr^2\pi\sqrt{\pi}} \exp\left(-\frac{3x^2}{r^2} - \frac{3y^2}{r^2} - \frac{3z^2}{h^2}\right) \quad , \qquad (4)$$

where $q(x, y, z)$ is the heat flux density of point (x, y, z) in the coordinate system, Q is the laser power, η is laser absorptivity of powder, r represents the radius of Gaussian laser beam, and h is the depth of Gaussian heat flux. The laser scanning direction and magnitude of heat source are controlled using a self-developed FORTRAN program.

According to the first law of thermodynamics, the thermal energy balance equation in the thermal model can be described as follows:

$$Q_L = Q_{cd} + Q_{cv} + Q_r \quad , \qquad (5)$$

where Q_L, Q_{cd}, Q_{cv}, and Q_r represent the total input energy, the energy transferred to powder layer, heat loss by convection, and radiant heat, respectively [22].

Combining the Fourier law and taking into account the local heating in the SLM process, the three-dimensional heat conduction equation with isotropic thermal properties used in the model can be written as follows:

$$\frac{\partial q}{\partial t} = \frac{k}{\rho C_P}\left(\frac{\partial^2 q}{\partial x^2} + \frac{\partial^2 q}{\partial y^2} + \frac{\partial^2 q}{\partial z^2}\right) \quad , \qquad (6)$$

where k is thermal conductivity coefficient in three directions, ρ is the powder bulk density, C_P is the specific heat, and q is the heat flux.

In the process of SLM simulation, the initial temperature of powder bed is assumed to be:

$$T(x,y,z)_{t=0} = T_0 \quad , \qquad (7)$$

where T_0 is set to 25 °C, which means the initial temperature of powder bed is consistent with ambient temperature.

During SLM process, considering the convection effect and heat radiation of material surface, the natural boundary conditions for heat transfer are characterized using a temperature-dependent comprehensive thermal parameters [23].

$$A = \begin{cases} 0.0668T & 0 < T < 500\ ^\circ\mathrm{C} \\ 0.231T - 82.1 & T > 500\ ^\circ\mathrm{C} \end{cases} \quad , \qquad (8)$$

where the unit of comprehensive thermal parameters (A) is $\frac{\mathrm{W}}{\mathrm{m}^2\ \mathrm{K}}$.

Material properties

In the finite element model of SLM process, the input thermal physical parameters of material has a great influence on the calculation accuracy; thus, temperature-dependent material properties are applied in this study and listed in Table II.

TABLE II: Thermal physical properties of GH3536 alloy used in the thermal model.

Temperature (°C)	Density (g/cm^3)	Specific heat [J/(g K)]	Conductivity [W/(m K)]
25	8.34	0.422	12.61
300	8.25	0.473	17.00
600	8.13	0.641	21.63
900	7.98	0.638	25.60
1200	7.82	0.665	30.10
1500	7.44	0.744	91.38

In addition, due to the particularity of powder bed, the thermal conductivity of powder bed is assumed to be one percent of the solid phase. To simulate the intense convective heat transfer effect located in the molten pool, the thermal conductivity of liquid phase is regarded as three times that of the solid phase. Many researchers have proven that the density of powder was supposed to be 40–60% of the solid phase, and the density of powder bed utilized in this study can be mathematically described as follows [24, 25]:

$$\rho_m = \frac{\pi}{6}\rho_s \quad , \qquad (9)$$

where ρ_s is the density of solid phase.

Finally, to attain sufficient simulation accuracy, the material state of the powder-to-solid transition is considered and realized through a self-developed FORTRAN program. In this thermal model, when the temperature of powder bed exceeds solid phase line under the effect of laser scanning, the powder material will be automatically updated with solid thermal properties and then keep solidification material state in the cooling process, thereby realizing the transformation between powder material and solidification alloy during SLM process.

Finite element model configuration

Finite element simulations are conducted to investigate the thermal field and molten pool dimension in the SLM of GH3536 alloy. A 3D finite element model used in this research is shown in Fig. 8. The model consists of a stainless steel substrate with a dimension of 1.40 × 0.80 × 0.20 mm and a powder bed of GH3536 with a dimension of 0.80 × 0.40 × 0.08 mm. The powder bed is divided into two layers and each layer is 40/70/100 μm thick. The bottom layer is used to eliminate the influence of substrate on thermal behavior and the top layer is applied to simulate SLM process. The laser scanning path is shown in Fig. 8 as well. To decrease simulation time and retain sufficient calculation accuracy, the powder layer is finely meshed with a 3D heat transfer element, whose dimension is equal to 0.0125 × 0.0125 × 0.0125 mm, while substrate applies coarser mesh, whose size is set to gradual

https://doi.org/10.1557/jmr.2019.7 Published online by Cambridge University Press

© Materials Research Society 2019

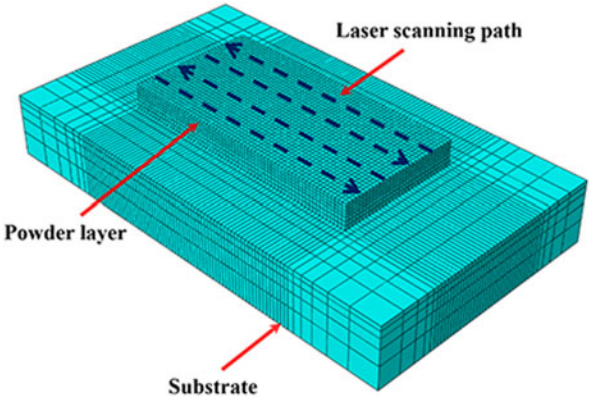


Figure 8: 3D finite element model for the SLM of GH3536 powder.

increase with the distance away from the scanning domain [26]. As a result, the three-dimensional simulation model in this research is meshed into 34,881 nodes and 30,296 elements in total.

Acknowledgments

This work was supported by the project to strengthen industrial development at the grass-roots level (Project No. TC160A310/19), Natural Science Foundation of Shanghai (Project No. 17ZR1409200), Shanghai Rising-Star Program (Project No. 18QB1400600), and Shanghai Industry Technology Institute Innovation Pioneer Program (Project No. 16CXXF006).

References

1. **H. Liu, X. Wang, D. Liu, Z. Wen, and Z. Yue**: Influence of notch on creep properties of GH3536 nickel-based superalloy. *Rare Met. Mater. Eng.* **43**, 2473 (2014).
2. **D. Herzog, V. Seyda, E. Wycisk, and C. Emmelmann**: Additive manufacturing of metals. *Acta Mater.* **117**, 371 (2016).
3. **T. DebRoy, H.L. Wei, J.S. Zuback, T. Mukherjee, J.W. Elmer, J.O. Milewski, A.M. Beese, A. Wilson-Heid, A. De, and W. Zhang**: Additive manufacturing of metallic components—Process, structure, and properties. *Prog. Mater. Sci.* **92**, 112 (2017).
4. **C.Y. Yap, C.K. Chua, Z.L. Dong, Z.H. Liu, D.Q. Zhang, L.E. Loh, and S.L. Sing**: Review of selective laser melting: Materials and applications. *Appl. Phys. Rev.* **2**, 041101 (2015).
5. **H. Ali, H. Ghadbeigi, and K. Mumtaz**: Effect of scanning strategies on residual stress and mechanical properties of selective laser melted Ti6Al4V. *Mater. Sci. Eng., A* **712**, 175 (2018).
6. **T. Rong, D.D. Gu, Q.M. Shi, S.N. Cao, and M.J. Xia**: Effects of tailored gradient interface on wear properties of WC/Inconel 718 composites using selective laser melting. *Surf. Coat. Tech.* **307**, 418 (2016).
7. **D.D. Gu, Y.C. Hagedron, W. Meiners, G.B. Meng, R.J.S. Batista, K. Wissenbach, and R. Poprawe**: Densification behavior, microstructure evolution, and wear performance of selective laser melting processed commercially pure titanium. *Acta Mater.* **60**, 3849 (2012).
8. **L. Thijs, F. Verhaeghe, T. Craeghs, J. Van Humbeeck, and J.P. Kruth**: A study of the micro structural evolution during selective laser melting of Ti–6Al–4V. *Acta Mater.* **58**, 3303 (2010).
9. **Z. Chen, Z.Y. Wei, P. Wei, S.G. Chen, B.H. Lu, J. Du, J.F. Li, and S.Z. Zhang**: Experimental research on selective laser melting AlSi10Mg alloys: Process, densification and performance. *J. Mater. Eng. Perform.* **26**, 1 (2017).
10. **B. Song, S.J. Dong, B.C. Zhang, H.L. Liao, and C. Coddet**: Effects of processing parameters on microstructure and mechanical property of selective laser melted Ti6Al4V. *Mater. Des.* **35**, 120 (2012).
11. **Y.C. Bai, Y.Q. Yang, D. Wang, and M.K. Zhang**: Influence mechanism of parameters process and mechanical properties evolution mechanism of maraging steel 300 by selective laser melting. *Mater. Sci. Eng., A* **703**, 116 (2017).
12. **G.Q. Yu, D.D. Gu, D.H. Dai, M.J. Xia, C.L. Ma, and Q.M. Shi**: On the role of processing parameters in thermal behavior, surface morphology and accuracy during laser 3D printing of aluminum alloy. *J. Phys. D: Appl. Phys.* **49**, 135501 (2016).
13. **C. Luo, J.H. Qiu, Y.G. Yan, J.H. Yang, C. Uher, and X.F. Tang**: Finite element analysis of temperature and stress fields during the selective laser melting process of thermoelectric SnTe. *J. Mater. Process. Technol.* **261**, 74 (2018).
14. **Y. Li and D.D. Gu**: Parametric analysis of thermal behavior during selective laser melting additive manufacturing of aluminum alloy powder. *Mater. Des.* **63**, 856 (2014).
15. **K. Moussaoui, W. Rubio, M. Mousseigne, T. Sultan, and F. Rezai**: Effects of selective laser melting additive manufacturing parameters of Inconel 718 on porosity, microstructure and mechanical properties. *Mater. Sci. Eng., A* **735**, 182 (2018).
16. **F. Wang, X.H. Wu, and D. Clark**: On direct laser deposited Hastelloy X: Dimension, surface finish, microstructure and mechanical properties. *Mater. Sci. Technol.* **27**, 344 (2011).
17. **J. Song, W.H. Wu, L. Zhang, B.B. He, L. Lu, X.Q. Ni, Q.L. Long, and G.L. Zhu**: Role of scanning strategy on residual stress distribution in Ti–6Al–4V alloy prepared by selective laser melting. *Optik* **170**, 342 (2018).
18. **J. Goldak, A. Chakravarti, and M. Bibby**: A new finite element model for welding heat sources. *Metall. Mater. Trans. B* **15**, 299 (1984).
19. **J. Goldak, M. Bibby, J. Moore, R. House, and B. Patel**: Computer modeling of heat flow in welds. *Metall. Mater. Trans. B* **17**, 587 (1986).

https://doi.org/10.1557/jmr.2019.7 Published online by Cambridge University Press

© Materials Research Society 2019

20. **B. Song, S.J. Dong, H.L. Liao, and C. Coddet**: Process parameter selection for selective laser melting of Ti6Al4V based on temperature distribution simulation and experimental sintering. *Int. J. Adv. Des. Manuf. Technol.* **61**, 967 (2012).
21. **J.R. Zhuang, Y.T. Lee, W.H. Hsieh, and A.H. Yang**: Determination of melt pool dimensions using DOE-FEM and RSM with process window during SLM of Ti6Al4V powder. *Opt. Laser Technol.* **103**, 59 (2018).
22. **I.A. Roberts, C.J. Wang, R. Esterlein, M. Stanford, and D.J. Mynors**: A three-dimensional finite element analysis of the temperature field during laser melting of metal powders in additive layer manufacturing. *Int. J. Mach. Tool Manufact.* **49**, 916 (2009).
23. **C.H. Lee, K.H. Chang, and J.U. Park**: Three-dimensional finite element analysis of residual stresses in dissimilar steel pipe welds. *Nucl. Eng. Des.* **256**, 160 (2013).
24. **K. Antony, N. Arivazhagan, and K. Senthilkumaran**: Numerical and experimental investigations on laser melting of stainless steel 316L metal powders. *J. Manuf. Process.* **16**, 345 (2014).
25. **R.B. Patil and V. Yadava**: Finite element analysis of temperature distribution in single metallic powder layer during metal laser sintering. *Int. J. Mach. Tool Manufact.* **47**, 1069 (2007).
26. **B. Cheng, S. Shrestha, and K. Chou**: Stress and deformation evaluations of scanning strategy effect in selective laser melting. *Addit. Manuf.* **12**, 240 (2016).

https://doi.org/10.1557/jmr.2019.7 Published online by Cambridge University Press

© Materials Research Society 2019